Quantification of diffraction artifacts in subsalt images caused by top-salt velocity errors

Guillaume Barnier and Biondo Biondi

ABSTRACT

We present an approach to identify and quantify patterns in migrated subsalt images caused by small-scale velocity errors in the vicinity of the top-salt interface. These velocity anomalies, which behave as point diffractors, generate artifacts in subsalt reflectors that have coherent moveout information. We show that the signature of a given velocity error in the image is the same as the impulse response of a migration with one source at the surface and a single virtual receiver placed at the velocity error location. Our final goal is to use the moveout information of these patterns to gradually extract them from the image and translate them into velocity model updates (close to the salt interface) by applying a wave equation migration velocity analysis (WEMVA) optimization scheme.

INTRODUCTION

One of the main bottlenecks for subsalt imaging is the limitation of currently existing techniques that accurately delineate the interface between the top of a salt body and its overlying sediments. A slight misinterpretation of this interface can significantly damage the image-quality of potential hydrocarbon-bearing subsalt layers. Modeling the salt-sediment boundary and resolving its very fine-scale features with accuracy remains challenging because this interface is usually very rugose and may take complex geometrical shapes. Moreover, the image-quality of underlying reflectors is extremely sensitive to the accuracy of the boundary location. Even a small error easily generates incoherent subsalt images (Etgen et al., 2014a,b; Barnier and Biondi, 2015).

When wavefields cross the salt-sediment interface, high wavenumber anomalies present at the boundary tend to behave as point diffractors, thereby generating diffraction "tails" in the recorded data. If our salt velocity model is inaccurate and does not contain such fine-scale features, these diffraction tails do not recollapse correctly when migrating the data. Instead, they generate undesirable artifacts in the image space that largely contribute to the loss of coherency.

We show that the undesired events in the image (created by small velocity errors at the salt boundary) contain coherent moveout information that we can quantify directly from migrated images on a shot-by-shot basis. Each small-scale velocity error generates an artifact in the image that is equivalent to the output of a migration with

the current shot position as a source and a single receiver located at the unknown position of the missing diffractor near the salt interface. For constant velocity medium, we present analytical expressions that model the shape of such a response in time-lag extended images. This allows us to scan the partially migrated images and extract these artifacts from them. Our next direction is to take a similar approach as in Sava and Biondi (2004) by gradually removing the errors from the image and generating appropriate image residuals that are robust enough to avoid cycle-skipping issues.

ORIGIN AND QUANTIFICATION OF DIFFRACTION ARTIFACTS IN SUBSALT IMAGES

We explain the origin and the mechanism of the artifacts in migrated images when the top-salt velocity model contains small-scale inaccuracies (i.e., errors with dimensions on the order of the wavefield dominant wavelength). First, we illustrate the concept with a simple test. Then, we show that if we consider a migrated image computed for one shot (with the source at the surface), the shapes of these artifacts can be approximated as the superposition of impulse responses of migrations with the same source, but receivers located at the position of the unknown top-salt velocity errors.

Uncollapsed diffraction tails

If wavefields pass through small-scale anomalies, diffraction "tails" are generated and recorded in the data. If the medium is isotropic, these tails have spherical shapes (in the (x, y, z)-space), whose centers are located in the vicinity of the anomalies that created them. If the data is back-propagated in time using the correct velocity model (i.e., the one containing the anomalies), these spheres recollapse toward their centers, and their energy is greatly attenuated. However, if the velocity model is inaccurate, these events re-expand and lead to the presence of artifacts in the image.

To illustrate this issue, we consider a *transmission* problem shown in Figure 1 where we burry a point source at $z_s = 0.9$ km, and $x_s = 0.5$ km. Data is recorded using 200 receivers at the surface, spaced every 5 m. We place two anomalies in a constant background velocity medium of 1.5 km/s. The dimensions of the anomalies are on the order of the wavefield dominant wavelength (approximately 80 m). We use a 30-Hz Ricker wavelet as the source. The recorded data is shown in Figure 2(a). It contains the direct event (green arrows) and the diffraction tails coming from the scattering of the direct wavefield as it passes through the anomalies (red arrows). As a comparison, Figure 2(b) displays the recorded data obtained without the anomalies, which does not contain any diffraction event. Figure 3 shows a set of snapshots of the adjoint wavefields (recorded data, back-propagated in time). The snapshots on the left column show the adjoint wavefield computed with the correct velocity model. The diffraction tails present at later times collapse as the wavefront reaches the anomalies, and most of their energy is cancelled out after that. The right column

shows the adjoint wavefield computed for a constant velocity medium (without the anomalies). In that case, the diffraction tails collapse when the wavefield reaches the anomalies but expand again as the wavefield propagates backward in time toward greater depths.

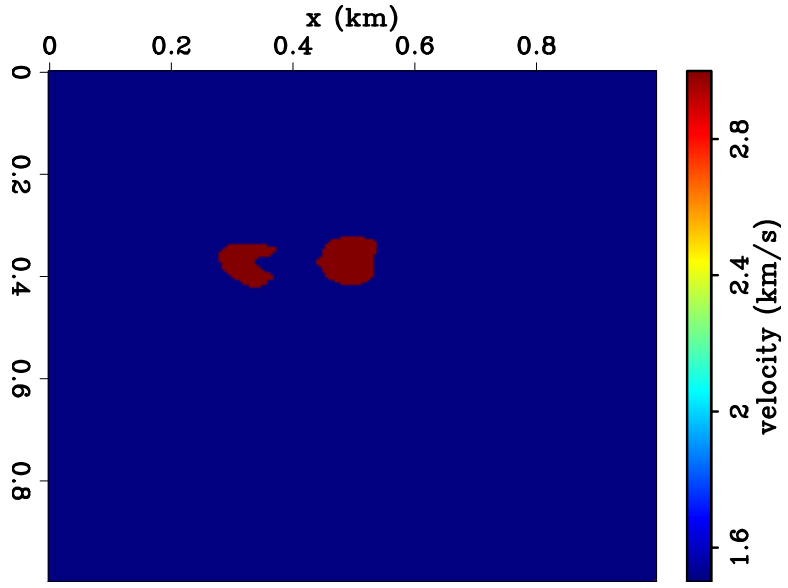

Figure 1: True velocity model. [**NR**]

In a subsalt imaging problem, the uncollapsed diffraction tails in the adjoint wavefield generate artifacts in the migrated image (of subsalt layers) that decrease its coherency. Therefore, we are interested in estimating the shape or moveout of these artifacts in the image space (i.e., after cross-correlation with the source wavefield).

Mechanism of diffraction artifacts in the image space

In order to quantify the contribution of diffraction tails in migrated subsalt images, let us consider the migration for one shot (with the source at the surface) and let us assume that our velocity model only contains small-scale errors at the sediment-salt boundary (and not bulk velocity errors).

As mentioned in the previous section, the back-propagated "receiver" wavefield is contaminated by diffraction tails that cross-correlate with the source wavefield and generate incoherent contributions to the image. By linearity of the cross-correlation operator, the migrated image for this shot is the sum of two images: (1) the "main" wavefront cross-correlated with the source wavefield, and (2) the diffraction tails cross-correlated with the source wavefield, which gives rise to the undesired artifacts that contaminate our image. We believe the image contribution of the source wavefield with wavefield (1) is what provides the coherent information in the final image.

Wavefield (2) is problematic. It propagates between the top-salt and potential

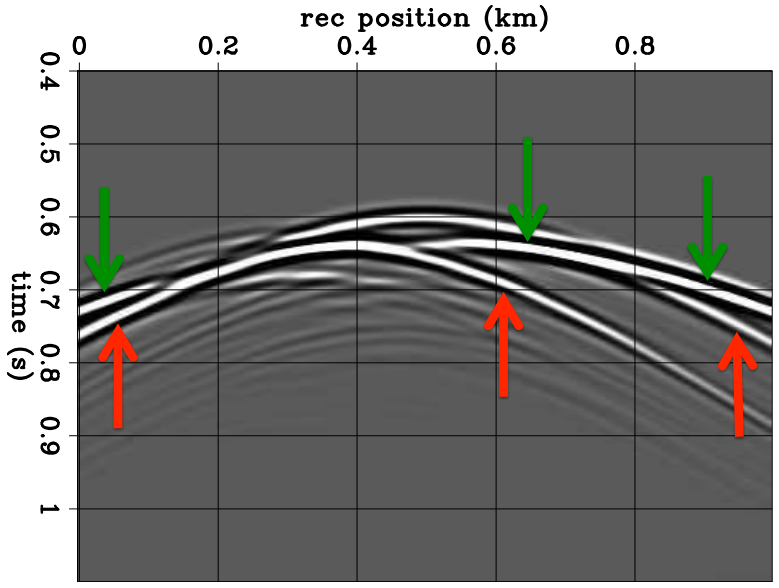

(a)

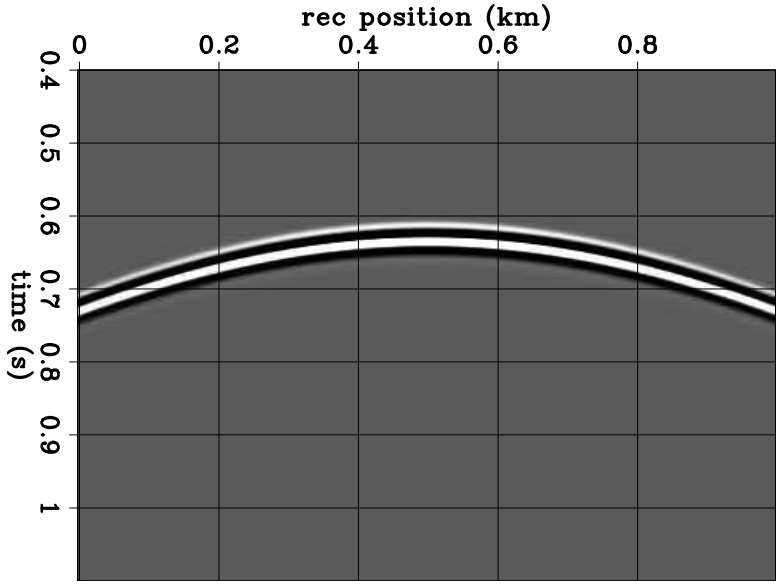

(b)

Figure 2: Recorded data at the surface generated by a point source burried at ($z_s = 0.9$ km, $x_s = 0.5$ km), and receivers at the surface. (a) Data computed using velocity model shown in Figure 1. (b) Data computed using the constant background velocity model, without the anomalies. [**ER**]

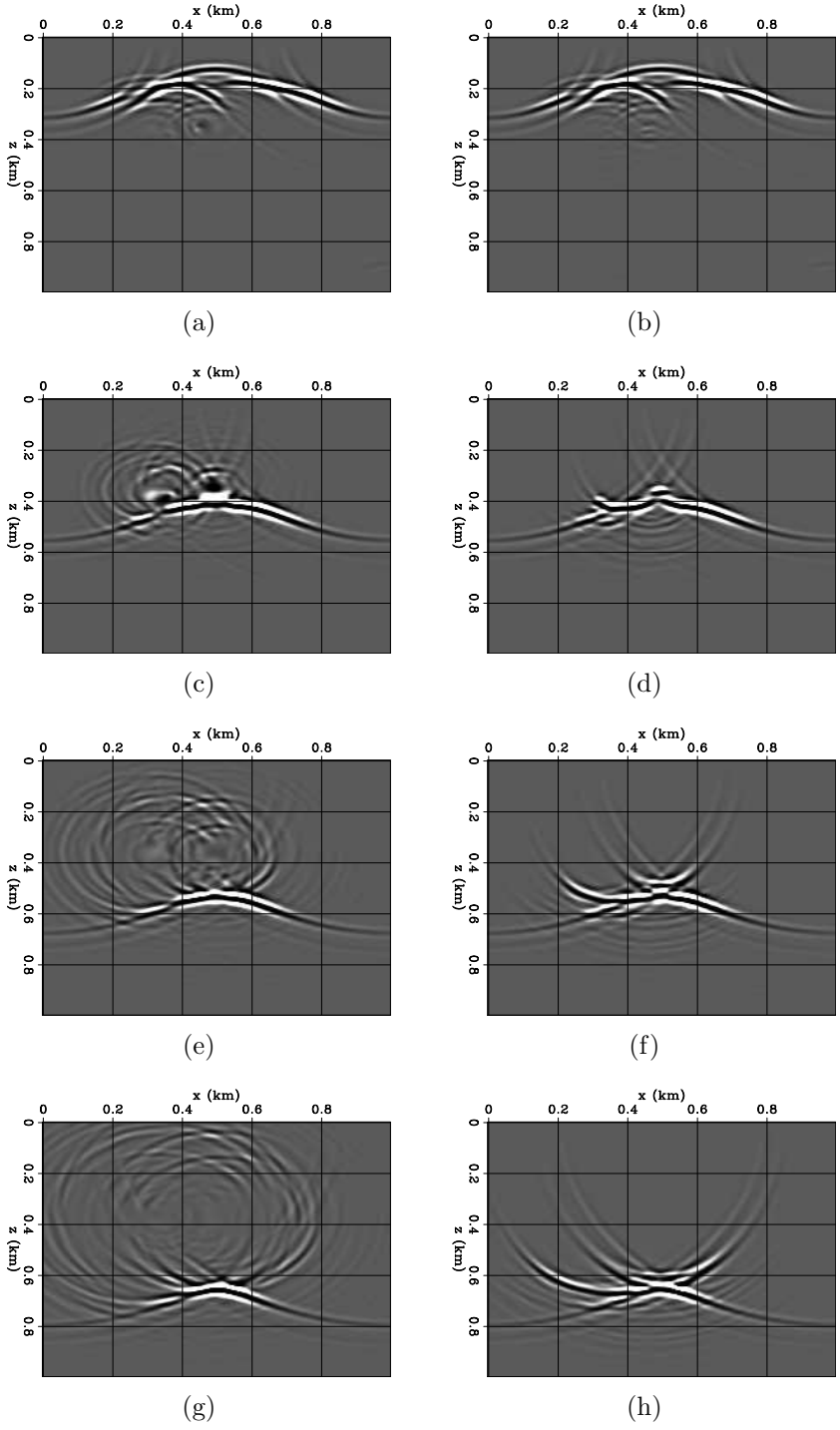

Figure 3: True velocity model. Snapshots of adjoint wavefields (data back-propagated in time) extracted at $t_4 = 0.520$ s (first row), $t_3 = 0.360$ s (second row), $t_2 = 0.280$ s (third row), and $t_1 = 0.200$ s (fourth row). Left column shows the ideal adjoint wavefield. Right column shows the wavefield computed with the wrong velocity model. All figures are displayed with the same color scale. [**ER**]

underlying reflectors as if it had been generated by a point source at the location of the missing feature in our model (near the salt-sediment interface). Therefore, the image contribution caused by this velocity error is the image we would obtain if we were to perform a migration of a band-limited impulse in time (recorded at time t_{col} when the wavefield tail recollapses at the point diffractor) with one source (the one giving rise to the source wavefield for this specific shot) and one single receiver located at the unknown position of the diffractor at the salt boundary. For instance, in a constant velocity medium and for a two-dimensional space, the image contribution would be an ellipse whose foci are located at the source and at the missing diffractor. Note that the shape of the ellipse is independent of the sign of the velocity error at the salt boundary (as long as it is "small").

Diffraction artifacts moveout in a constant velocity medium

Now that we understand how diffraction events caused by a misinterpretation of the salt boundary translate into migrated images, we quantify them with an analytical expression for a two-dimensional space. We can also broaden this quantification to time-lags extended images. The purpose is to use this analytical expression to scan the migrated image for such events, isolate them, and eventually back-project them in our model space using a WEMVA inversion scheme.

We consider the migration impulse response of an event recorded at time t_r at a receiver $R(x_r, z_r)$, excited by a source $S(x_s, z_s)$. We choose a coordinate system such that $z_s = z_r = 0$ km, and we compute the response for time-lag extended images. The time-lag extended imaging condition can be written in the discretized form as follows (Sava and Fomel, 2006):

$$I(x, z, \tau) = \sum_{t=0}^{N_t} P_s(x, z, t-\tau) P_r(x, z, t+\tau), \tag{1}$$

where I is the time-lag extended image, and P_s and P_r are the source and receiver wavefields, respectively. τ denotes the time-lag applied to the source and receiver wavefields. The impulse response of such a migration is the set of points in the (x, z, τ)-space that satisfy the following equation (modified from Claerbout and Green (2008)):

$$\frac{(x-x_c)^2}{A^2} + \frac{z^2}{A^2-h^2} = 1, \tag{2}$$

where $x_c = \dfrac{(x_r + x_s)}{2}$ is the coordinate of the midpoint between S and R, v is the medium velocity, t_r is the time at which the event was recorded, $A = \dfrac{v}{2}(t_r - 2\tau)$,

and $h = \dfrac{|x_r - x_s|}{2}$ is the half-distance between S and R. For a constant time-lag, the response is an ellipse whose focus points are located at S and R, with major semi-axis A, and minor semi-axis $B = \sqrt{A^2 - h^2}$. Note that both semi-axes decrease as τ increases. For a constant depth, the migration response is the set of points that also satisfy Equation 2, which can be rearranged as follows:

$$\gamma^2 - \gamma\beta - (h^2 + z^2)\gamma + \beta h^2 = 0, \tag{3}$$

where $\gamma = \dfrac{v^2}{4}(t_r - 2\tau)^2$, and $\beta = (x - x_c)^2$. It can be shown that the set of points in the (γ, β)-plane that satisfy Equation 3 are located on a hyperbola with center C_h whose coordinates are (h^2, z^2).

Application to subsalt imaging

To first order, we use the diffraction moveout characterization derived for constant velocity medium to identify diffraction patterns in partially migrated subsalt images. Our first analysis is only based on non-extended images in a two-dimensional space. For each image, we search for the presence of ellipses or elliptical-shaped artifacts. We choose to parametrize each ellipse in the following way:

- The first focus point is the (known) source position $S(x_s, z_s)$
- The second focus point is the (unknown) position of the missing diffractor $M_d(x_d, z_d)$
- The major semi-axis $A = \dfrac{v}{2} t_{\text{col}}$, where v is the medium velocity and t_{col} is the time at which the diffraction tail (of the receiver wavefield) collapses at the scattering location near the salt boundary

We are therefore left with three unknown parameters to characterize each ellipse: the diffractor horizontal position x_d, the diffractor depth z_d, and the major semi-axis A. By selecting a range of possible values for each of those parameters, we can then scan the image by summing along elliptical trajectories, and map each ellipse back to the (x_d, z_d, A)-space, by minimizing the following objective function:

$$\mathbf{m}_s^* = \text{argmin } ||\text{E}\mathbf{m}_\text{s} - \text{I}_\text{s}||_2^2, \tag{4}$$

where $\mathbf{m}_s = (x_d, z_d, A)^T$ is the ellipse parametrization, I_s is the partial image computed for shot s, and E is a spreading operator along elliptical trajectories (linear

with respect to $\mathbf{m}_s$). For each shot, we can then compute an image residual expressed by:

$$\Delta I_s = \mathrm{E}\mathbf{m}_\mathrm{s}^*, \tag{5}$$

and back-project the total image residual $\Delta I = \sum_{s=1}^{N_s} \Delta I_s$ into a velocity model update using a WEMVA scheme.

SYNTHETIC EXAMPLE

To illustrate our method, we consider a synthetic subsalt imaging problem. The true velocity model, shown in Figure 4(a), is a modified version of the BP 2004 benchmark velocity model. We assume a constant and known overburden velocity model (displayed in blue). Our goal is to image the flat reflector located at a depth $z_{\mathrm{ref}} = 1.485$ km (displayed in light blue in Figure 4(a)). We use an inaccurate background velocity model shown in Figure 4(b) containing a misinterpreted top-salt. The velocity error is displayed in Figure 4(c). We use a finite-difference scheme to model wavefields, with a grid spacing of 15 m by 15 m. The wavefields are generated using a 20-Hz Ricker wavelet. The dominant wavelength is approximately $\lambda_{\mathrm{sed}} \approx 75$ m in the overlying sediment layer and $\lambda_{\mathrm{salt}} \approx 150$ m in the salt (displayed in red). The dimensions of the velocity model errors range from 50 m to 200 m. We set 180 sources at the surface, spaced every 60 m, and 720 receivers (also at the surface) every 15 m. Imaging is performed using a two-way wave-equation acoustic and constant density engine.

We migrate the recorded data for 180 shots using the inaccurate background velocity model. The image of the reflector is of poor quality in the (x, z)-plane (Figure 5(a)) as well as in the (x, τ)-plane (Figure 5(b)). In Figure 5(a), the "smiles" (located slightly above the reflector image) appear to be overmigration artifacts. In fact, they are caused by the stacking of partial images contaminated by the diffraction events, whose moveout can be approximated by ellipses. Similarly, we can also recognize the signature of such events in the (x, τ)-plane.

Figures 6 and 7 show migrated sections for only one shot located at $x = 1.5$ km. Due to the shot position, we only display the section up to $x_{\mathrm{max}} = 4$ km, which is where most of the energy is located. In Figure 6(b), we can clearly see artifacts in the image coming from the incorrect top-salt delineation, which seem to have elliptical shapes. Moreover, the diffraction artifacts also seem to show some moveout similar to what we would obtain according to Equation 3 in the (x, τ)-plane (Figure 7(b)). By looking at the receiver wavefield, we can also identify the origin of the diffraction artifact present in the image. Figure 8 shows five snapshots of the receiver wavefields back-propagated in time. Left column is the receiver wavefield computed with the true velocity model, and right column shows the one computed with the inaccurate

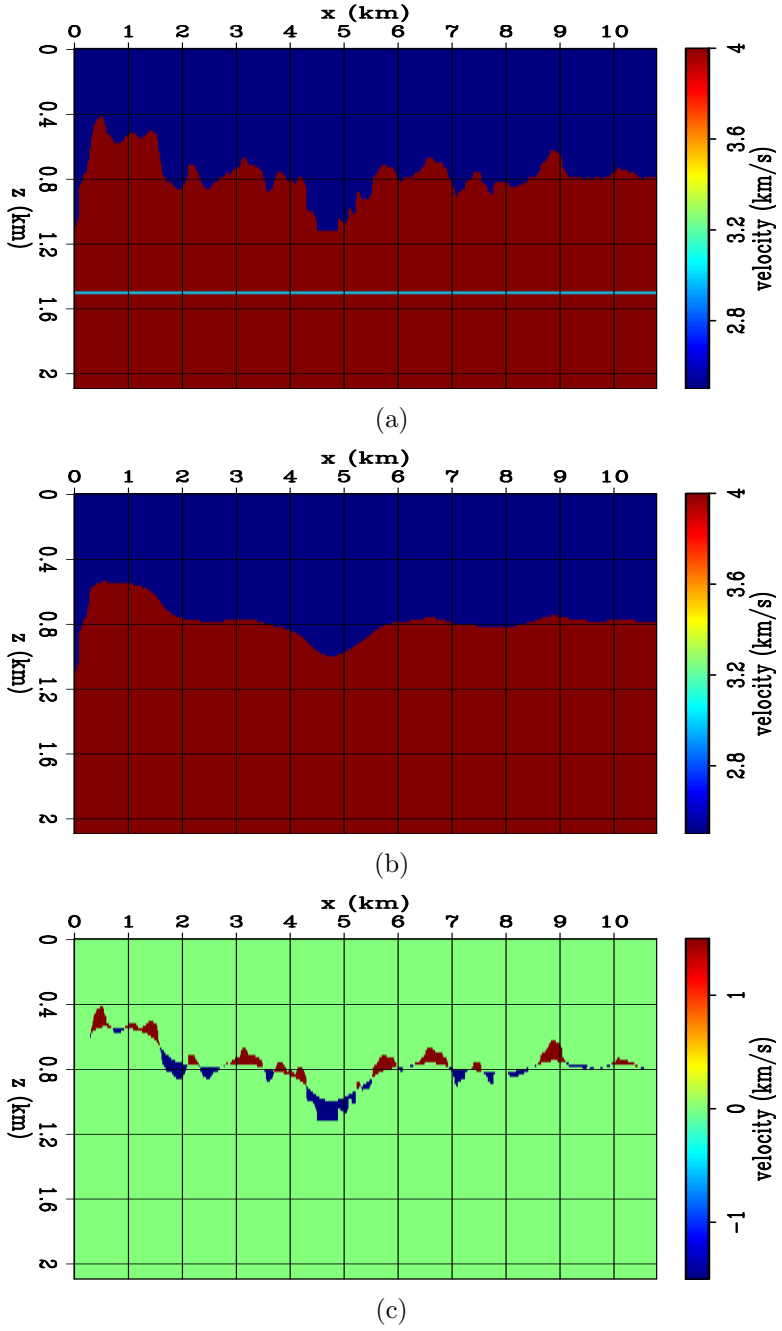

Figure 4: (a) True velocity model, modified from the BP 2004 benchmark model. (b) Inaccurate top-salt velocity model. (c) Velocity error. [**NR**]

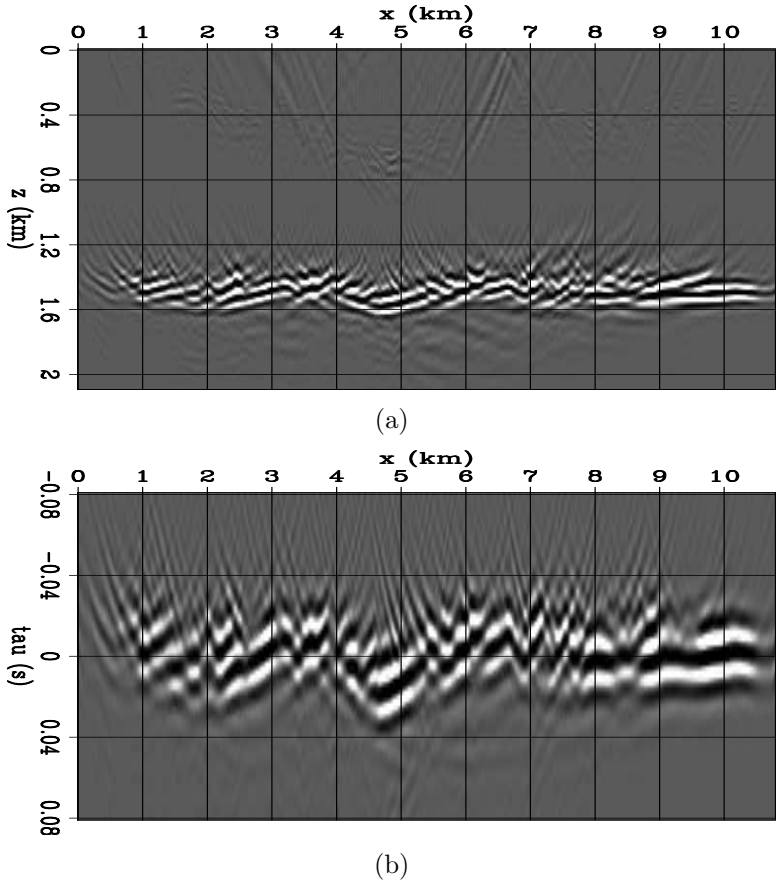

Figure 5: Migrated images computed using the inaccurate background model shown in Figure 4(b). (a) Image displayed in the (x, z)-plane at zero time-lag ($\tau = 0$ s). (b) Image displayed in the (x, τ)-plane at a constant depth $z = z_{ref}$. [**CR**]

background model. On the right column, we can identify three major uncollpased diffractions whose centers are located at approximately $M_1(x_1 = 3 \text{ km}, \text{z}_1 = 0.8 \text{ km})$, $M_2(x_2 = 1.5 \text{ km}, \text{z}_2 = 0.8 \text{ km})$, and $M_3(x_3 = 0.5 \text{ km}, \text{z}_3 = 0.6 \text{ km})$, which corresponds to the position of velocity errors in the incorrect background model (Figure 9).

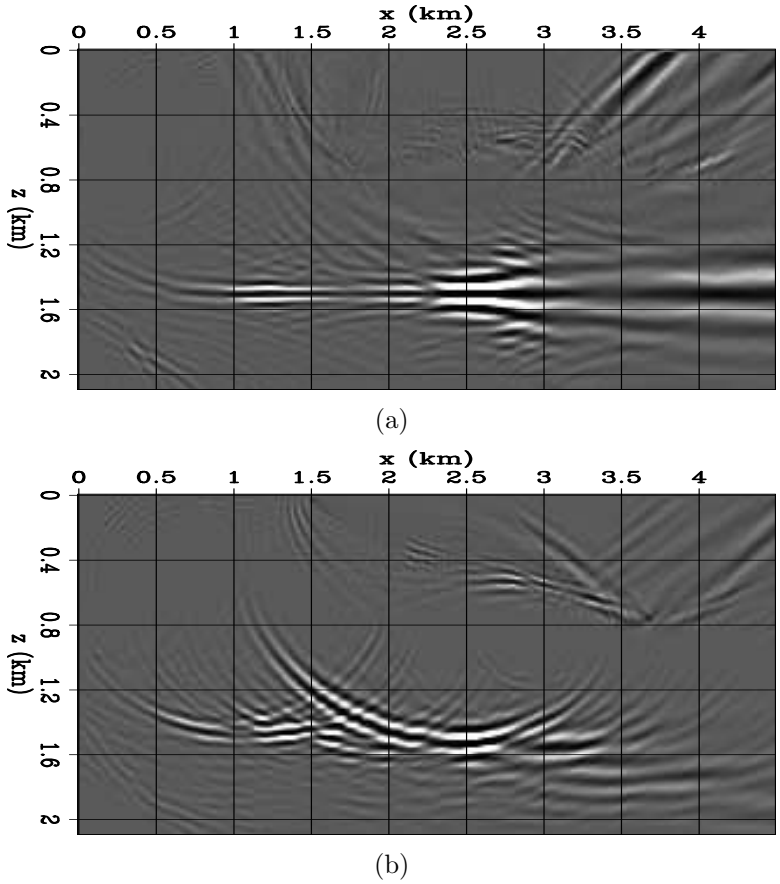

(a)

(b)

Figure 6: Migrated images for one shot (positioned at $x = 1.5$ km and $z = 0$ km) displayed in the (x, z)-plane and extracted at a constant time-lag $\tau = 0$ s. (a) Migration using the correct velocity model. (b) Migration using the inaccurate velocity model. Both images are displayed on the same color scale. [**ER**]

For this specific shot, we solve the inverse problem proposed in Equation 4. The inverted model in the (x_r, z_r, A)-space is displayed in Figure 10. Each panel corresponds to a semblance plot (obtained by summing along ellipses) displayed as a function of the unknown diffractor horizontal position x_r and depth z_r and given a fixed value of the major semi-axis A of the ellipse. The scanning range for the diffractor depth z_r is determined by limiting its possible values within a window centered around the top-salt interface. We are able to identify zones of high energy but as expected, the location of the scattering position is not well constrained with respect to the major semi-axis value A (Figure 10(a)-(c)) as many combinations of (x_r, z_r, A) points can produce the same elliptical shapes in our image. Figure 10(d) shows no match for such a high value of A. If we compute the image residual for this shot

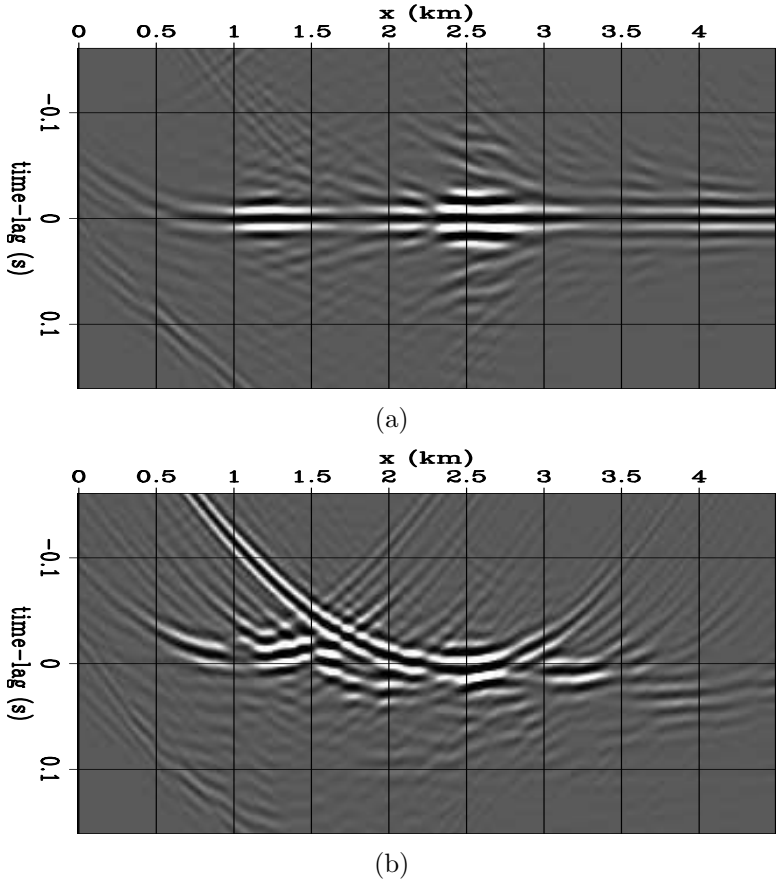

Figure 7: Migrated images for one shot (positioned at $x = 1.5$ km and $z = 0$ km) displayed in the (x, τ)-plane and extracted at a constant depth $z_{ref} = 1.485$ km. (a) Migration using the correct top-salt. (b) Migration using the inaccurate velocity model. Both images are displayed on the same color scale. [**ER**]

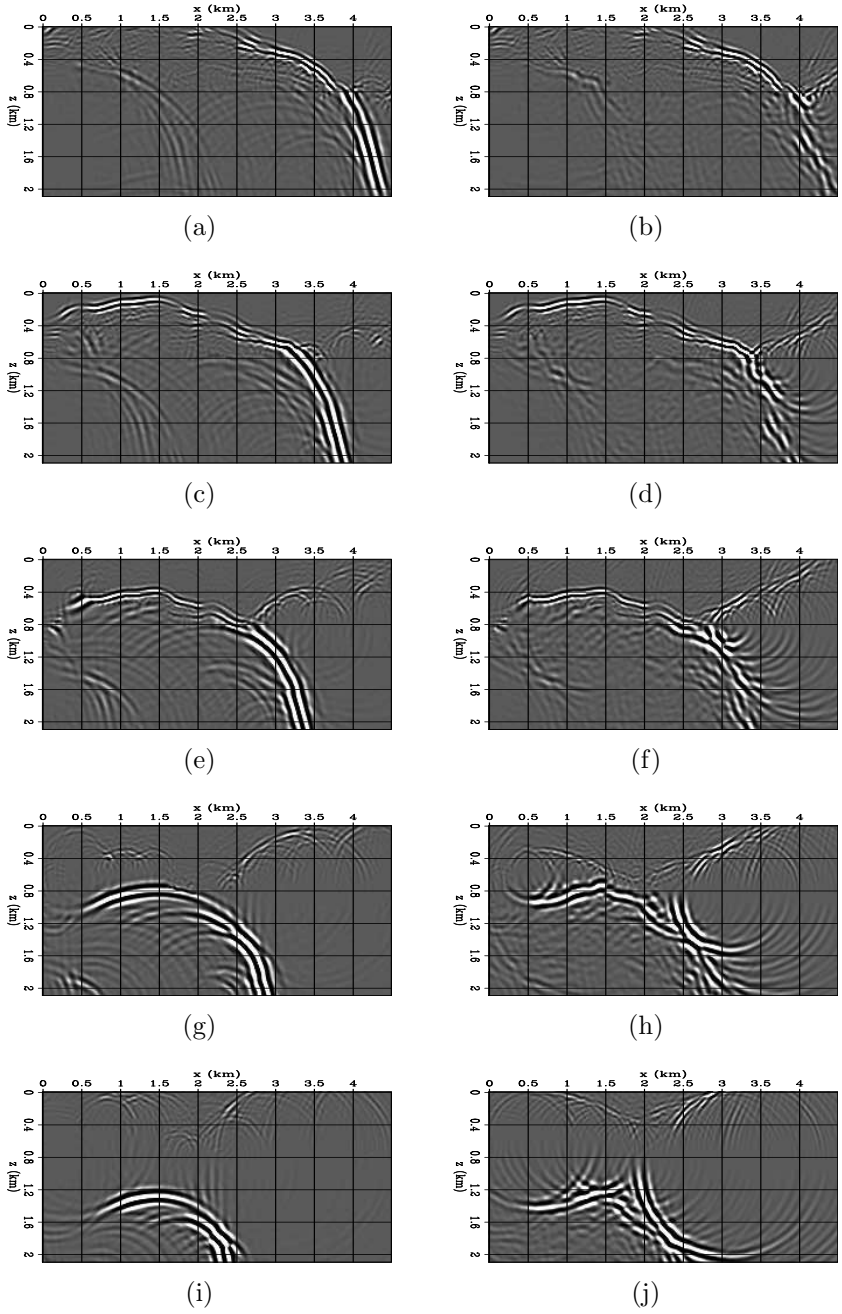

Figure 8: Snapshots of the ideal (left column) and inaccurate (right column) back-propagated receiver wavefields. Snapshots are extracted at $t_5 = 1.080$ s (first row), $t_4 = 0.960$ s (second row), $t_3 = 0.840$ s (third row), $t_2 = 0.720$ s (fourth row), $t_2 = 0.600$ s (fifth row). All figures are displayed with the same color scale. [**ER**]

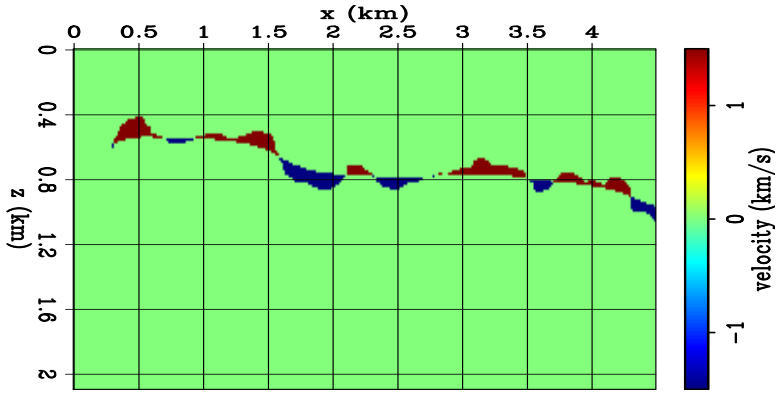

Figure 9: Close up of the velocity error shown in Figure 4(c). [**NR**]

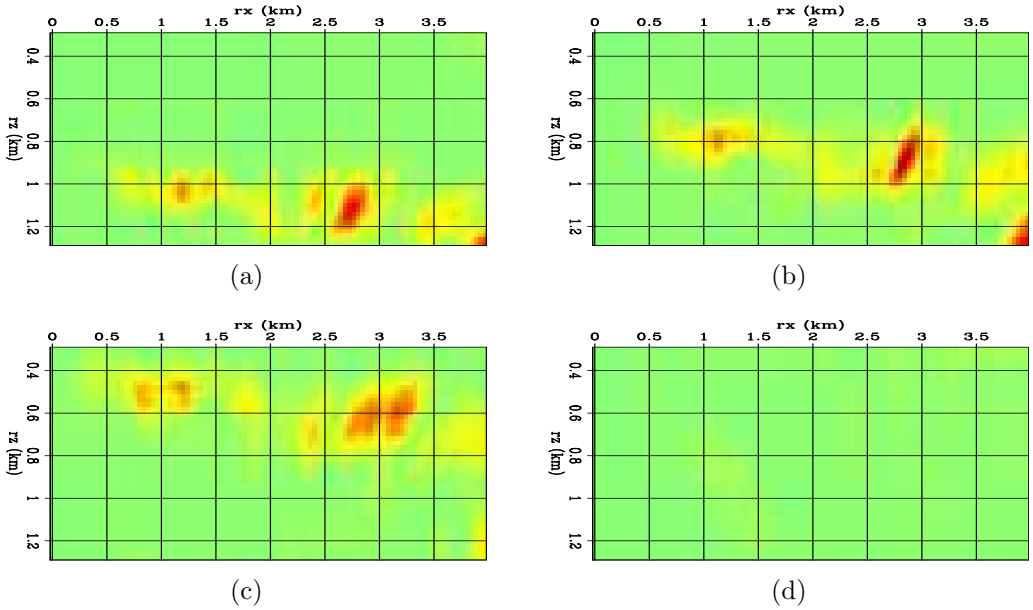

Figure 10: Inverted model in the (x, τ)-plane for four different values of the major semi-axis A. (a) $A = 0.76$ km. (b) $A = 0.96$ km. (c) $A = 1.16$ km. (d) $A = 1.56$ km. [**ER**]

(Equation 5), we can see that it matches the original image quite well (Figure 11). It captures most of the energy of the original image, except for flat events. However, the scanning results strongly depend on the parameters' scanning range. For instance, a flat and correctly imaged reflector can also appear as part of an ellipse with realistic parameters (given the source position for this shot), and can be seen as an "artifact". Therefore, even though this first approach manages to capture some of the elliptical features for this specific example, it still lacks robustness. It needs to be better constrained in order to only extract energy corresponding to uncollapsed diffractions artifacts.

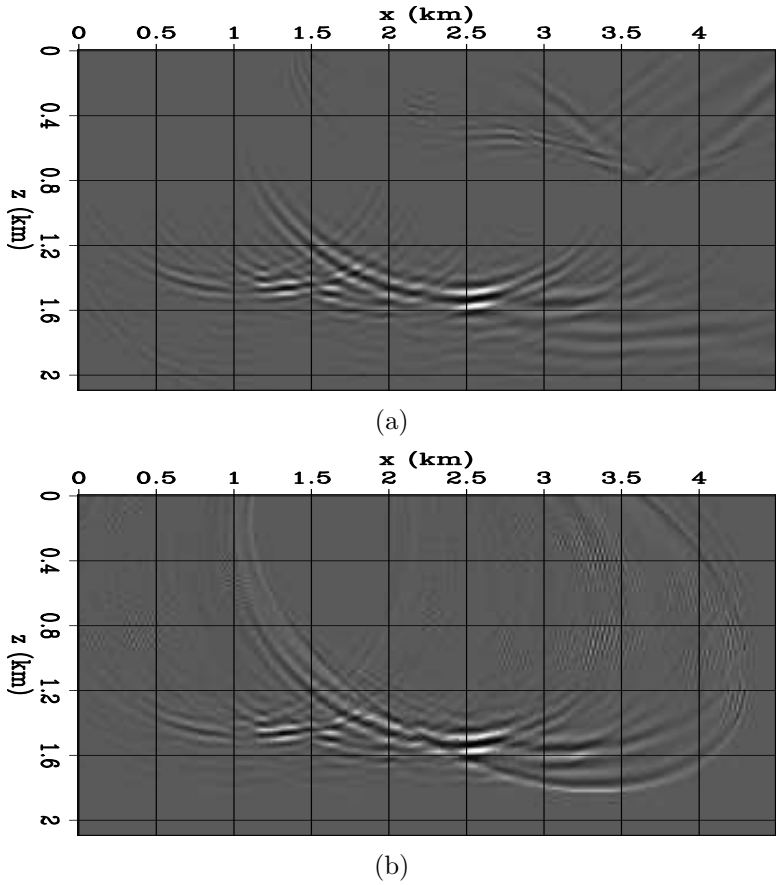

Figure 11: (a) Partially migrated image using the incorrect velocity model. (b) ΔI_s, which corresponds to the inverted model $\mathbf{m}_s$ projected in the image space. Figures are displayed on the same color scale. [**ER**]

CONCLUSIONS AND FUTURE DIRECTIONS

Top-salt small-scale velocity errors in our model can cause artifacts in the image space, making the total migrated subsalt images incoherent. We showed that diffraction events generated by the passage of wavefields across the rugose salt boundary are not attenuated correctly because of the missing features in our velocity model.

For a given shot, we managed to model their signature (or moveout) in the time-lag extended image space. It is the superposition of migrated images using one source at the surface and receivers at the location of the velocity errors. Our first approach was to scan the partially migrated images for patterns (ellipses in the (x, z)-plane) that approximately matched the signature of the diffraction artifacts. Though encouraging, this approach lacks robustness and needs to be improved. It can potentially be done by adding bound constrains on the proposed scanning inversion, enforcing sparsity in the inverted model using an L1-norm scheme, and using moveout information from time-lag extended images.

Once the diffraction artifacts can be automatically extracted from migrated images, we will focus on developing an operator similar to the one derived in Sava and Biondi (2004), where the image perturbations (i.e., image residuals) are "manipulated" to ensure that they are consistent with the Born approximation (Sava and Biondi, 2004). Our operator should be able to capture the curvature of the diffraction moveout in the (x, z, τ)-space and *gradually* correct these events in a WEMVA inversion scheme.

ACKNOWLEDGMENTS

We would like to thank the Stanford Exploration Project affiliate companies for financial support. Guillaume Barnier especially thanks Gustavo Alves, Ettore Biondi, T.J. Dahlke, and Joe Stefani for useful discussions and advice.

REFERENCES

Barnier, G. and B. Biondi, 2015, Addressing the effects of inaccurate top-salt delineation on subsalt seismic imaging: SEP-Report, **158**, 67–102.

Claerbout, J. F. and I. Green, 2008, Basic earth imaging: Citeseer.

Etgen, J. T., I. Ahmed, M. Zhou, et al., 2014a, Seismic adaptive optics: Presented at the 2014 SEG Annual Meeting.

Etgen, J. T., C. Chu, T. Yang, M. Vyas, et al., 2014b, Adaptive image focusing: Presented at the 2014 SEG Annual Meeting.

Sava, P. and B. Biondi, 2004, Wave-equation migration velocity analysis. i. theory: Geophysical Prospecting, **52**, 593–606.

Sava, P. and S. Fomel, 2006, Time-shift imaging condition in seismic migration: Geophysics, **71**, S209–S217.